

Cometary ion dynamics at 67P: A collisional test-particle approach with Rosetta data comparison

Z. M. Lewis,^{1,2}★ P. Stephenson,³ A. Beth,¹ M. Galand,¹ E. Kallio,⁴ and A. Moeslinger⁵

¹*Department of Physics, Imperial College London, UK*

²*Lancaster University, Bailrigg, UK*

³*Lunar and Planetary Laboratory, Tucson, AZ, USA*

⁴*Aalto University, Helsinki, Finland*

⁵*Umeå University, Umeå, Sweden*

Accepted XXX. Received YYY; in original form ZZZ

ABSTRACT

The Rosetta spacecraft escorted comet 67P/Churyumov-Gerasimenko for two years, gathering a rich and variable dataset. Amongst the data from the Rosetta Plasma Consortium (RPC) suite of instruments are measurements of the total electron density from the Mutual Impedance Probe (MIP) and Langmuir Probe (LAP).

At low outgassing, the plasma density measurements can be explained by a simple balance between the production through ionisation and loss through transport. Ions are assumed to travel radially at the outflow speed of the neutral gas. Near perihelion, the assumptions of this field-free chemistry-free model are no longer valid, and plasma density is overestimated. This can be explained by enhanced ion transport by an ambipolar electric field inside the diamagnetic cavity, where the interplanetary magnetic field does not reach.

In this study, we explore the transition between these two regimes, at intermediate outgassing ($5.4 \times 10^{26} \text{ s}^{-1}$), when the interaction between the cometary and solar wind plasma influences the transport of the ions. We use a 3D collisional test-particle model, adapted from Stephenson et al. (2022) to model the cometary ions with input electric and magnetic fields from a hybrid simulation for 2.5–3 au. The total plasma density from this model is then compared to data from MIP/LAP and to the field-free chemistry-free model. In doing so, we highlight the limitations of the hybrid approach and demonstrate the importance of modelling collisional cooling of the electrons to understand the ion dynamics close to the nucleus.

Key words: comets: individual: comet 67P/CG – plasmas

1 INTRODUCTION

The cometary ionosphere is formed by the ionisation of the neutral coma, expanding neutral gas released by sublimating ices from the nucleus. Unlike at planets, these ions are not gravitationally bound, but are instead continuously produced and lost to space.

The ion environment of Comet 67P/Churyumov-Gerasimenko was explored extensively by the ESA Rosetta mission during its main escort phase (Glassmeier et al. 2007a). Amongst the large and varied payload was the Rosetta Plasma Consortium (RPC) suite of instruments (Carr et al. 2007), designed to measure the charged particle populations and to shed light on the comet-solar wind interaction. In this study, we use electron density data from the Mutual Impedance Probe (MIP, Trotignon et al. (2007)) and the Langmuir Probe (LAP, Eriksson et al. (2007)).

1.1 Ionospheric chemistry

For most of the Rosetta escort, the neutral coma of 67P was primarily comprised of water, that can be directly ionised by solar photons,

electron impact, or solar wind charge exchange, to produce H_2O^+ . When the coma is dense enough, H_2O^+ is quickly lost through the transfer of a proton to H_2O , forming H_3O^+ :



This reaction happens so readily that H_3O^+ is often the dominant ion species in the cometary coma (e.g. Murad & Bochsler (1987), Heritier et al. (2017b)). If the outgassing is high enough, H_3O^+ can then be lost to reactions with high proton affinity neutrals (Altwegg et al. (1993), Vignen & Galand (2013), Heritier et al. (2017b)). These are neutrals for which it is energetically favourable to ‘steal’ a proton from H_3O^+ , and this process can happen repeatedly for neutrals with increasing proton affinity until the terminal ion, whose associated neutral has the highest proton affinity, is reached. The terminal ion is then lost through transport or ion-electron dissociative recombination. The neutral with the highest proton affinity in the coma of 67P is NH_3 , leading to the formation of its protonated version, NH_4^+ (Altwegg et al. (1993), Vignen & Galand (2013)):



NH_4^+ can also be produced through interaction between NH_3 and other protonated versions of neutrals with proton affinity higher than water but lower than NH_3 . Therefore, although H_3O^+ is usually

★ E-mail: zoe.lewis@lancaster.ac.uk

the dominant ion species, when the coma is dense enough for ion-neutral chemistry to happen more readily, NH_4^+ can overtake it. Only a small mixing ratio of NH_3 in the neutral population is required for significant production of NH_4^+ . Since it can only be produced through ion-neutral chemistry, and not directly through ionisation, NH_4^+ is a useful indicator that the timescale for ion-neutral chemistry is similar to or less than the timescale for ion transport (Vigren & Galand (2013), Heritier et al. (2017b), Beth et al. (2019)). NH_4^+ can hence be used as a tracer of ion-neutral chemistry occurring in the coma

NH_4^+ has been detected at 67P by the ROSINA-DFMS (Rosetta Orbiter Spectrometer for Ion and Neutral Analysis - Double-Focussing Mass Spectrometer, Balsiger et al. (2007)) using the high mass-resolution mode (Beth et al. 2016). Detections increase with outgassing, and the ion is more prevalent near perihelion (Heritier et al. (2017b), Lewis et al. (2023)), where the coma is more dense and ion-neutral reactions can happen more efficiently. Lewis et al. (2023) showed that DFMS counts of NH_4^+ are greater inside the diamagnetic cavity - the magnetic field-free region surrounding the nucleus, sporadically detected by the RPC magnetometer (MAG, Glassmeier et al. (2007b), Goetz et al. (2016)). This correlation between the diamagnetic cavity and NH_4^+ demonstrates the link between the plasma dynamics and the ion composition.

1.2 Plasma density driven by ion dynamics

The simplest parameters we can use to describe the cometary ion population are the total ion density n_i (which is approximately equal to the total electron density n_e , since quasi-neutrality is maintained in the plasma), and the ion bulk velocity \vec{u}_i . These parameters are inextricably linked, and tied together by the continuity equation

$$\frac{\partial n_i}{\partial t} + \nabla \cdot (n_i \vec{u}_i) = (\nu^{hv} + \nu^{e^-}) n_n - R_{DR} n_e \quad (3)$$

where ν^{hv} and ν^{e^-} are the photo-ionisation and electron-impact ionisation frequencies, respectively. n_n is the density of the neutral coma, which can be expressed by a simplified Haser model (Haser 1957) as $n_n = Q / (4\pi u_n r^2)$, where u_n is the neutral expansion velocity and Q , m the total outgassing rate. R_{DR} is the effective loss rate of the ions due to ion-electron dissociative recombination.

For large heliocentric distances and close to the comet, Galand et al. (2016) demonstrated that a simple balance between the ionisation rate and radial ion transport was sufficient to explain the RPC-MIP and RPC-LAP electron density. For such a low outgassing (at < 3 au), the following conditions were determined to be valid:

- No attenuation of the incoming solar EUV (coma is optically thin),
- No plasma loss through dissociative recombination ($R_{DR} = 0$)

Further to this, a simplifying assumption was made: that the cometary ions travel radially outwards at the same speed as the neutrals. Under these conditions the continuity equation (Eq. 3) can be solved to find that the ion density n_i is simply

$$n_i = \frac{(\nu^{hv} + \nu^{e^-}) n_n}{u_n} (r - r_c) \quad (4)$$

where r_c is the approximate radius of the nucleus. A comparison of the plasma density calculated using Eq. 4 and from RPC/MIP and RPC/LAP measurements is shown in Figure 1. A similar comparison was made in Vigren et al. (2019), but we now present an updated version with the combined LAP/MIP dataset (Johansson et al. 2021)

and including both photo- and electron-impact ionisation frequencies (Stephenson et al. 2023).

In general, this field-free chemistry-free model works well to explain the electron density at low outgassing post-perihelion (Heritier et al. (2017a), Heritier et al. (2018)) as well as pre-perihelion (Galand et al. 2016). The range of cometocentric distances probed by Rosetta at this time was usually within a few tens of kilometres from the surface, so the full parameter space could not be explored, but there is good agreement over the regions probed, which extended up to ~ 80 km post-perihelion (Heritier et al. 2018) (see Figure 1 after March 2016).

At higher outgassing ($Q \gtrsim 10^{27} \text{ s}^{-1}$), the plasma density is no longer well constrained by the simple model (see Vigren et al. (2019) and Figure 1). This is most likely due to the ions being accelerated by the ambipolar electric field such that $u_i \neq u_n$ (e.g. Vigren et al. (2017)). Lewis et al. (2024) showed through a 1D ionospheric model that acceleration of the ions by an electric field proportional to $1/r$, could be used to bring the modelled densities in line with those observed by RPC-MIP and RPC-LAP within the diamagnetic cavity. Outside the diamagnetic cavity, the non-zero magnetic field contributes to the convective and Hall terms (see e.g. Gunell et al. (2019), Beth & Galand (2017), Deca et al. (2019)) into the electric field, and the flow is no longer simply radial.

As demonstrated in Vigren et al. (2019), a transition occurs during late February to early March 2016 where the assumptions of the simple model become valid. Interestingly, the transition appears to coincide with the last observations of the diamagnetic cavity by RPC-MAG (Goetz et al. 2016) in mid February 2016. It is not known whether the diamagnetic cavity boundary lay below the spacecraft beyond these dates, but given the relatively short (and decreasing) distance of Rosetta from the comet nucleus it seems unlikely that the cavity persisted into March 2016.

Direct determination of the bulk ion velocity from Rosetta RPC measurements is possible, though challenging due the effect of the strongly negative spacecraft potential (Odelstad et al. 2017), and uncertainty in the ion temperature. Values of $2\text{--}8 \text{ km s}^{-1}$ have been derived using the current-voltage characteristics from RPC-LAP and the plasma density from RPC-MIP, using diamagnetic cavity crossings in August 2015 (Vigren et al. 2017) and November 2015 (Odelstad et al. 2018). Bergman et al. (2021b) used RPC-ICA energy spectra from 88 diamagnetic cavity crossings to derive bulk speed of $5\text{--}10 \text{ km s}^{-1}$, however the spacecraft potential distorts the measured direction and velocity of low energy ions from ICA, requiring disentangling with Particle-In-Cell simulations (Bergman et al. 2021a). Williamson et al. (2024) used a statistical approach, fitting drifting Maxwell-Boltzmann distributions to over 3000 RPC-ICA scans from across the whole Rosetta escort phase. They found that this produced consistently higher ion energies than those derived from RPC-LAP.

Despite some variations, all of these measurements suggest that the ion speed is higher than the neutral expansion speed u_n ($0.5\text{--}1 \text{ km s}^{-1}$, Biver et al. (2019), Hansen et al. (2016)), suggesting collisional decoupling between the ions and neutrals, and electric field acceleration of the ions. From 1D ion acceleration model simulations, Lewis et al. (2024) found that an electric field in r^{-1} of around 2 mV m^{-1} at the surface was sufficient to reproduce the plasma densities measured by RPC inside the diamagnetic cavity (for July and November 2015 case studies). Such a field would lead to bulk ion speeds at Rosetta of $1.4\text{--}3.0 \text{ km s}^{-1}$ in the diamagnetic cavity. However, the good agreement of the field-free chemistry-free model (Eq. 4) at lower outgassing (Galand et al. (2016), Heritier et al. (2018)) would suggest that an ion flow much closer to the neutral speed is dominant at larger heliocentric distances. One might expect

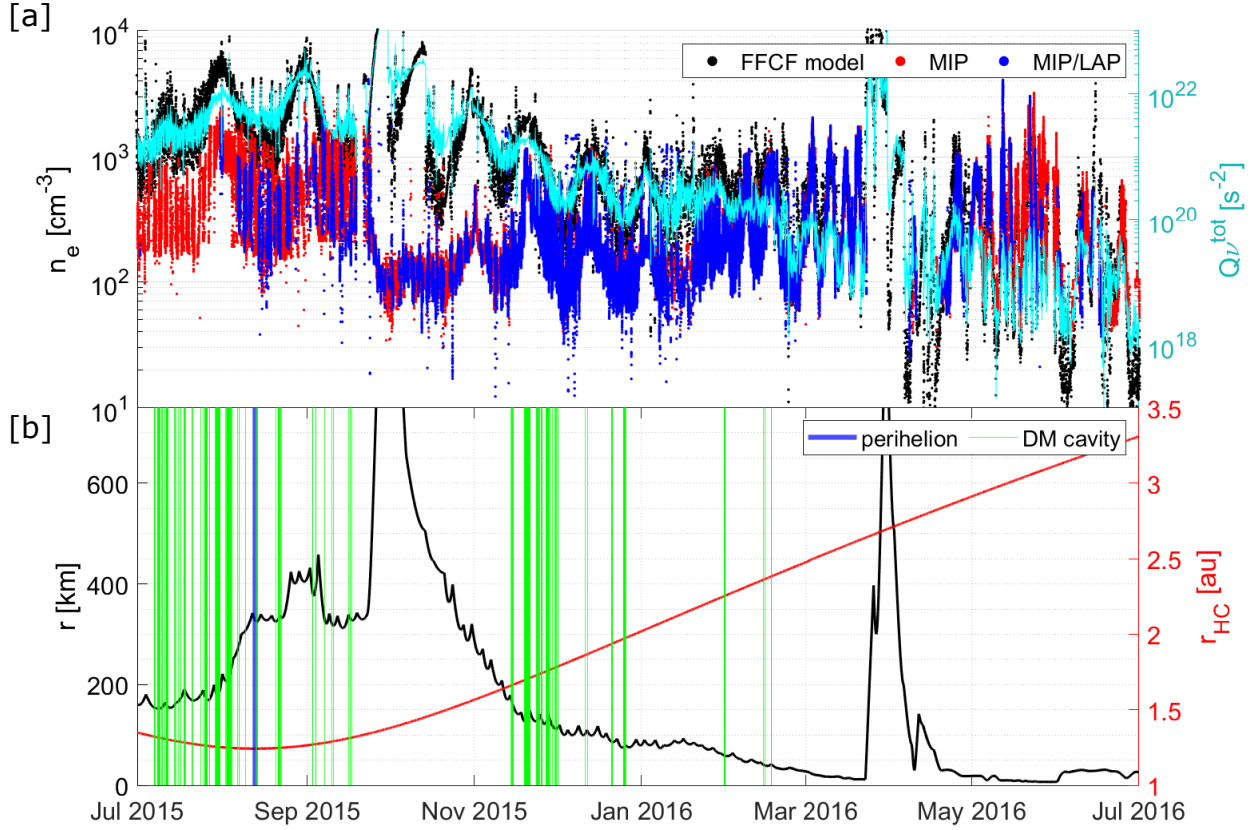


Figure 1. [a] Comparison of the (black) calculated plasma density from Eq. 4, with the measured electron density from (red) RPC-MIP and (blue) the MIP/LAP combined dataset (Johansson et al. 2021). (cyan) The ion production rate $Q\nu^{\text{tot}}$ where Q is the total outgassing rate calculated COPS and ν^{tot} is the sum of the total photoionisation and electron-impact frequencies (Stephenson et al. 2023). Data are shown for July 2015 - July 2016. [b] (black) cometocentric distance, and (red) heliocentric distance. Green lines mark diamagnetic cavity crossings (Goetz et al. (2016), width of line not to scale) and blue line indicates perihelion in August 2015.

that electric and magnetic fields are more likely to effect the ion velocity in the low outgassing regime, when there is no diamagnetic cavity and the solar wind's influence extends all the way to the surface. However, the good agreement of the $u_i = u_n$ model at low activity (Eq. 4) with the plasma density measurements is seemingly at odds with this.

Putting together this complex picture of the ion dynamics requires the ions to be treated kinetically, as is done in test-particle model and hybrid plasma simulations. Furthermore, detailed treatment of the ion-neutral collisions (i.e., to assess the extent of collisional decoupling) is key. This study aims to shed light on the effect of a more-complex 3D solar wind–comet interaction on the ionospheric composition and density, with a view to better interpret the RPC data for intermediate outgassing, between low outgassing conditions (Eq. 4) and the formation of a diamagnetic cavity (Lewis et al. 2024).

1.3 Structure of the paper

For this study, the collisional test-particle model originally developed for the electron populations around a comet (Stephenson et al. 2022)

has been adapted to instead describe the ion environment. We model the three key cometary ion species (H_2O^+ , H_3O^+ , and NH_4^+) and the collisions between them and the neutral coma background. In Section 2.1, the model is described and validated, with emphasis on the aspects of the code that were updated from the electron model. Section 2.3 describes the treatment of ion-neutral collisions in the model, including a comparison of the 3D kinetic approach and the 1D fluid approach to the diamagnetic cavity case presented in Lewis et al. (2024). Section 2.2 then describes the hybrid simulations that provide the electric and magnetic fields to drive the ions in the test-particle model.

Section 3 focuses on the cometary plasma environment around 67P at 2.5 – 3 au, when the outgassing was lower and the diamagnetic cavity was not detected. The density and bulk velocity of H_2O^+ , H_3O^+ , and NH_4^+ are assessed, highlighting the extent to which each is driven by the changing ion transport and collisions.

Finally, in Section 4, the combined dataset from MIP/LAP is compared with the results of the test-particle modelling in Section 3. The aim of this is to understand the drivers of the plasma density during the conditions used for the hybrid simulations, and to assess how well the simulation recreates them.

2 MODELLING

2.1 Collisional ion test-particle model

The test-particle model first described in [Stephenson et al. \(2022\)](#) was developed to assess the response of cometary and solar wind electron populations to electric and magnetic fields provided by a fully kinetic Particle-in-Cell (PiC) model ([Deca et al. \(2017\)](#), [Deca et al. \(2019\)](#)). Crucially, the test-particle approach enabled study of the effect of collisions on the overall electron environment, which have not yet been incorporated into kinetic PiC models ([Stephenson et al. \(2023\)](#), [Stephenson et al. \(2024\)](#)).

In this study, we have adapted the [Stephenson et al. \(2022\)](#) electron test-particle model to now model the cometary ion population. The model is described by the flow chart in Figure 2. First, the ions are created, either as photo-ions (H_2O^+) or as secondary ions (H_3O^+ , NH_4^+), produced through ion-neutral chemical reactions. H_2O^+ ions are initialised in the model with a given velocity and position in the grid. Newly produced ions originate from the neutral coma, they are initially given the same velocity as the neutrals: $\vec{u}_i = u_n \hat{r}$. The total unattenuated ionisation frequency $\nu_{\text{ioni}}^{\text{tot}}$ is supplied as an input to the model and subsequently calculated in 3D taking photo-absorption into account, using the Lambert-Beer law.

The simulated ions (macroparticles) represent a flow of ions that follow the same trajectory through the fields. H_2O^+ macroparticles are assigned a ‘weight’ (W_p), based on the number of ions per second which follow the same path. This weight is dependent on the number of other ions produced within the same grid cell. It is given by

$$W_p = \frac{1}{N_p} \int_{\text{cell}} \nu_{\text{ioni}}^{\text{tot}}(\vec{x}) n_n(\vec{x}) d^3\vec{x} \quad (5)$$

where N_p is the number of macroparticles produced within the cell and $n_n(\vec{x})$ is the neutral density at the position \vec{x} within the grid. The inner part of the production grid comprises of 20 small boxes ($1 \text{ km} \times 1 \text{ km} \times 1 \text{ km}$), extending from the origin, where the comet nucleus is centred. The rest of the ($1000 \text{ km} \times 1000 \text{ km} \times 1000 \text{ km}$) domain is then filled with logarithmically spaced boxes such that there are 50 cells in the x-direction (the comet-Sun line) and 40 in the y- and z-directions.

The particles are then pushed through the background fields by the Lorentz force. At each timestep, we check whether a collision has occurred, and if so, what type. Particles are terminated when they either leave the domain, hit the nucleus, or undergo a proton transfer. After the run for the photo-ions (H_2O^+) has been completed, the secondary ions are generated from the weights that have been saved when proton transfer collisions occur.

Finally, the moments of the distributions can be calculated based on the trajectories of the particles, provided enough particles have travelled through each cell. For details of the moment calculation, see [Stephenson et al. \(2022\)](#). The moments are calculated on a ($80 \times 60 \times 60$) cell grid with the same resolution as the electric and magnetic fields (25 km).

2.2 Hybrid electric and magnetic fields

The electric and magnetic fields are provided by AMITIS (Advanced Modelling Infrastructure in Space simulations, [Fatemi et al. \(2017\)](#)), a GPU-based 3D hybrid simulation that has been applied to various solar system bodies. The same run as presented in [Moeslinger et al. \(2024\)](#) is used. The ion production rate used as input to the AMITIS model run is $Q\nu = 1.08 \times 10^{20} \text{ s}^{-2}$, and corresponding Q and ν values for the test-particle model input are determined from the COPS data

Table 1. Inputs to the AMITIS hybrid simulation as used in Sections 3 and 4. The same inputs (where relevant) were applied to the test-particle model, except the moments were calculated over a $1000 \times 1000 \times 1000 \text{ km}$ grid.

$Q [\text{s}^{-1}]$	5.4×10^{26}
$\nu [\text{s}^{-1}]$	2×10^{-7}
$u_n [\text{km s}^{-1}]$	0.7
Simulation domain [km]	$7000 \times 12000 \times 16000$
Grid resolution [km]	25
Heliocentric distance [au]	$2.5 - 3$
Upstream $n_{\text{sw}} [\text{cm}^{-3}]$	1
Upstream $u_{\text{sw}} [\text{km s}^{-1}]$	430
Upstream $T_{e,\text{sw}} [\text{eV}]$	12
Upstream $B_{\text{IMF}} [\text{nT}]$	3

and total ionisation rates ([Stephenson et al. 2023](#)). The model inputs are summarised in Table 1, and are broadly representative of the conditions at 67P encountered by Rosetta at $2.5 - 3 \text{ au}$.

The electric and magnetic field magnitudes are shown in Figure 3. The Sun in the +X direction, and the interplanetary magnetic field is oriented along the +Y axis. The validation of the ion test-particle model under collisionless conditions is shown in Appendix A2, using the input parameters given in Table 1.

2.3 Ion-neutral collisions in 3D

Adapting the test-particle model to treat the cometary ion population requires a new set of cross sections. The full ion-neutral cross section set and references are presented in Appendix B. In general, the cross sections increase with decreasing relative energy, but the experimental cross sections are only available down to 0.1 eV. For relative energies below this value, values were linearly extrapolated in log space down to an approximate surface temperature of the neutrals of $\sim 0.01 \text{ eV}$ ([Heritier et al. \(2017b\)](#), [Marshall et al. \(2017\)](#)).

Dissociative recombination is neglected, which is justified at the outgassing rates used in this study ($10^{26} - 10^{27} \text{ s}^{-1}$, reflecting January–March 2016 during Rosetta). [Heritier et al. \(2018\)](#) demonstrated that neglecting recombination in this regime introduces less than 20% error (for $T_e = 200 \text{ K}$) in the total plasma density. This is even lower when acceleration of the ions by electromagnetic fields is taken into account (see [Lewis et al. \(2024\)](#)).

The probability of a given collision type c happening during a timestep dt is given by:

$$P_c(dt) = 1 - \exp[-n_n(\vec{x}) dV_\sigma] \quad (6)$$

where dV_σ is the volume ‘swept through’ by the collision cross section in the frame of the neutral gas (of relevant species, n). This volume is given by

$$dV_\sigma = \sigma_c(E_{\text{rel}}) v_{\text{rel}} dt \quad (7)$$

where v_{rel} is the relative speed between an ion and a neutral and the collision cross section is $\sigma_c(E_{\text{rel}})$.

For a neutral gas with a Maxwell velocity distribution function $f_n(\vec{v}_n)$, a bulk velocity \vec{u}_n , and a temperature T_n , the relative speed is defined as ([Fahr & Mueller 1967](#)):

$$v_{\text{rel}} = \iiint |\vec{v}_i - \vec{v}_n| f_n(\vec{v}_n) d^3\vec{v}_n. \quad (8)$$

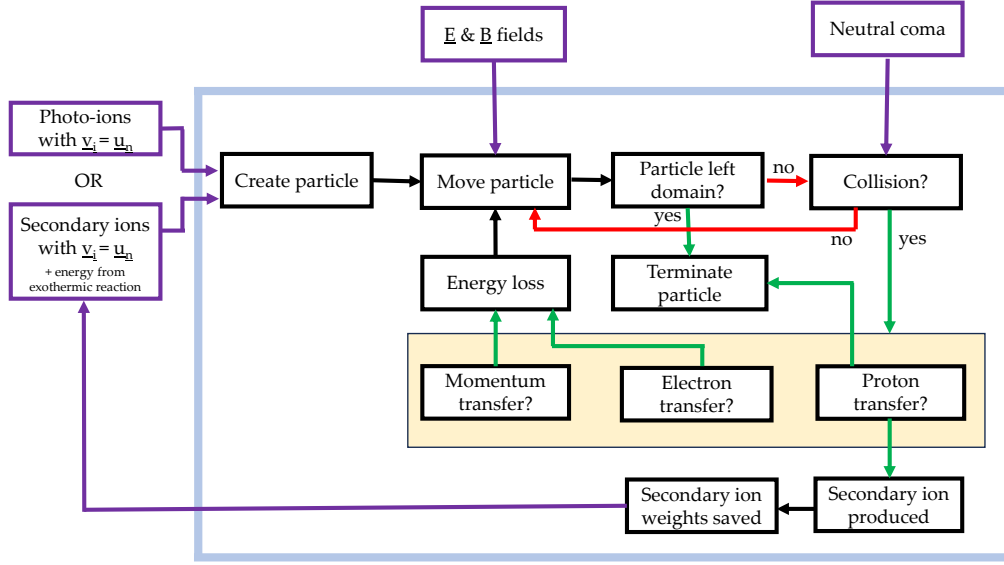


Figure 2. Flow chart representing the key elements of the ion test-particle model. The blue box separates processes happening inside the code, and the inputs controlled externally (in purple boxes). Adapted from [Stephenson et al. \(2022\)](#) for the application to cometary ions.

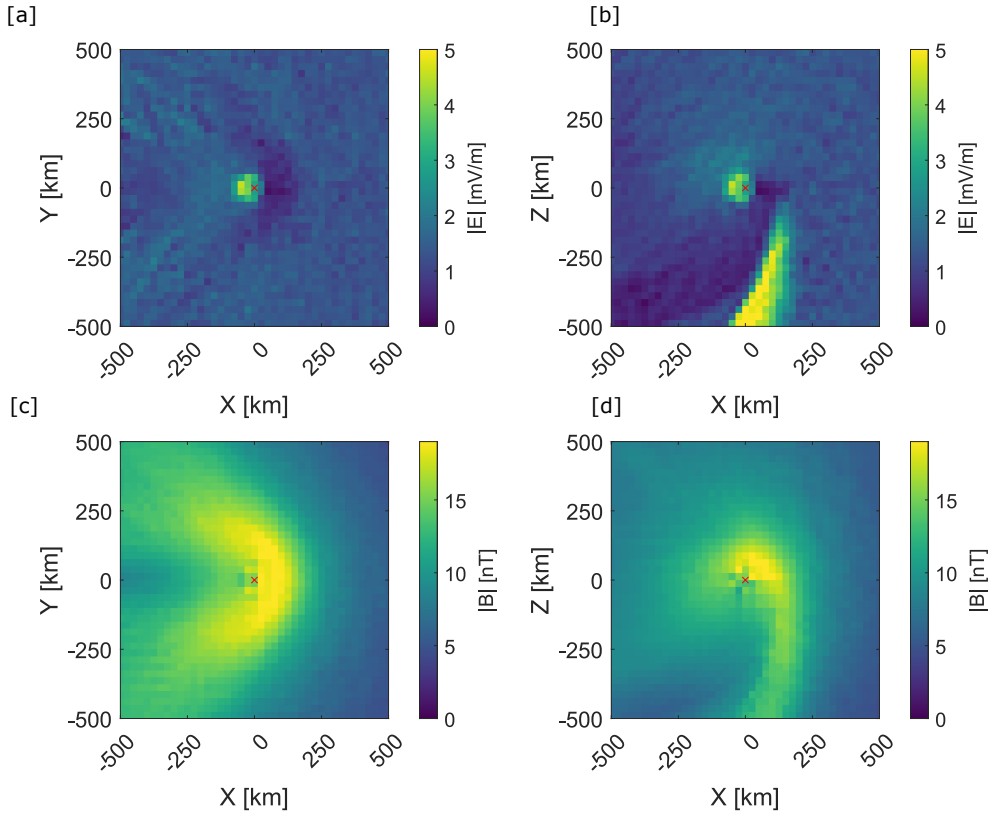


Figure 3. [a] and [b] Electric field and [c] and [d] magnetic field magnitudes from AMITIS ([Fatemi et al. 2017](#)), used to drive the collisional test-particle model ([Moeslinger et al. 2024](#)). Red cross indicates the position of the cometary nucleus.

Table 2. Inputs used to compare the 1D ion acceleration model and present test-particle model in Section 2.3.1. Inputs are data-based and justified in Lewis et al. (2024).

Rosetta equivalent date	2015-11-21
Q [s^{-1}]	7×10^{27}
ν [s^{-1}]	2×10^{-7}
%NH ₃	0.2
u_n [$km\ s^{-1}$]	0.75
$E(r_c)$ [$mV\ m^{-1}$]	0.5

Eq. 8 can be approximated as

$$v_{rel} \approx \left(\frac{4v_{n,th}^2}{\pi} + w_{rel}^2 \right)^{\frac{1}{2}} = \left((v_{n,th}^{mean})^2 + w_{rel}^2 \right)^{1/2} \quad (9)$$

where $v_{n,th} = \sqrt{\frac{2k_B T_n}{m_n}}$ is the location of the peak of the Maxwellian velocity distribution (in the frame of the gas), that is, the most probable speed. v_{rel} is a function of both the difference between the bulk velocities, $w_{rel} = |\vec{v}_i(\vec{x}) - \vec{u}_n(\vec{x})|$, and the thermal speed, $v_{n,th}^{mean}$, corresponding to the mean speed in the frame of the neutral gas. Eq. 9 is equivalent within 5% over all w_{rel} to the full solution to Eq. 8. v_{rel} can then be used to calculate the relative energy E_{rel} in order to find the cross section $\sigma_c(E_{rel})$ using

$$E_{rel} = \frac{1}{2} \frac{m_j m_n}{m_j + m_n} v_{rel}^2. \quad (10)$$

The 3D model allows us to account for the exothermic energy release from the protonation reaction. In this case, a component of velocity with a magnitude equivalent to the 0.5 eV energy release (Hunter & Lias 1998) is given to secondary ions (those newly produced through protonation) in a randomly generated direction.

The model has been validated using the energy-independent kinetic rates as used in the 1D ion acceleration model of Lewis et al. (2024), with the inputs given in Table 2. The validation is shown in Appendix A1.

2.3.1 1D fluid vs 3D kinetic modelling: diamagnetic cavity

The 3D kinetic approach can be used to assess the validity of the 1D fluid approach, applied within the diamagnetic cavity by Lewis et al. (2024). To do so, the hybrid electric and magnetic field inputs are replaced with $\vec{B} = \vec{0}$ everywhere in the simulation, and a radial electric field which is given by $\vec{E} = (E_c r_c / r) \hat{r}$, with $E_c = 0.5 \times 10^{-3} Vm^{-1}$ the field strength at the comet surface. The electric field is calculated over a $(1000 \times 1000 \times 1000)$ km grid with a 10 km spatial resolution in each direction. Since there is no magnetic field in this case, only a radial electric field, the set-up is valid only inside the diamagnetic cavity, and represents inputs similar to those seen on 21st November 2015 by Rosetta, illustrated in Table 2.

The implication of these energy-dependent cross sections on the ion composition and velocity profiles is shown in Figure 4. Overall, the main effect of the 3D treatment is to boost the proton transfer, reducing the H_2O^+ density and producing more NH_4^+ . This is because the energy-dependent cross sections peak at low energies. The total plasma density is increased by a factor of up to 1.3 in the 3D model thanks to more effective collisions, and the ion bulk velocity is up to 23% slower. However, as demonstrated in Lewis et al. (2024), the product $n_i u_i$ for a given r is preserved, so the determination of the electric field strength and bulk velocity that are required to recreate the measured plasma density from RPC-LAP and RPC-MIP remains valid.

Figure 4 also shows effect of an 0.5 eV exothermic energy release during protonation (solid line). The difference is very small (in some cases not visible on the plots), only reducing the total plasma density by a maximum of 5%, and increasing the bulk velocity by up to 8%.

3 COMETARY ION DYNAMICS AT 2.5-3 AU

We now run the full collisional ion test-particle simulation, driven by the hybrid electric and magnetic fields (input parameters in Table 1, see Section 2.2), representing comet 67P at 2.5-3 au. The neutral coma is assumed to be H_2O -dominated, with a 0.2 % contribution of NH_3 . The three ion species are H_2O^+ , H_3O^+ , and NH_4^+ (see Section 2.1).

Figure 5 shows the modelled ion density in the X-Y plane, with the Sun in the +X direction. Comparing Figure 5a (no collisions) and Figure 5b (collisions), the inclusion of collisions increases the total ion density, and the ions are slowed down.

The ion density is largest close to the nucleus, as in the 1D case, but it is also enhanced just inside the region of magnetic pile up (see Figure 3c). The cometary ions appear to stagnate in this area, which was also observed in the collisionless simulations of Moeslinger et al. (2024), but the addition of ion-neutral collisions increases the piled-up density. Figure 6 shows the ratio between the total ion density in the collisional and non-collisional case, in all three planes. Collisions are shown to increase the total ion density by up to 4 times, with the greatest impact on the densities in the region of ion pile up, on the inner edge of the magnetic pile up region. It can also be seen in Figure 6b that the effect of collisions is more significant for -Z values. This is likely due to enhanced transport in the +Z direction by the motional electric field.

When the ion density is separated into species (see Figure 5c-e), there is a clear difference in behaviour of the three key ion species. As ionisation and protonation processes are predominant in the inner coma, all three ion species are produced near the nucleus with a similar velocity to the neutral gas. However, all species are affected differently by the electric field. This is not simply because of different electromagnetic forces on them, since they all have the same charge (+e) and very similar masses (18–19 u q^{-1}). Instead, the difference in their ion-neutral chemical timescales drives this variation.

H_2O^+ (Figure 5c) is around an order of magnitude less prevalent and significantly more homogenous than H_3O^+ (Figure 5d), with no clear enhancement in the pile up region. H_2O^+ reacts very quickly with H_2O to form H_3O^+ , therefore it has too little time to undergo significant acceleration by the electric field. H_2O^+ is at (or close to) photochemical equilibrium in regions close to the nucleus, and directly lost through transport far from the nucleus.

NH_4^+ (Figure 5e) is produced in low densities (with similar magnitudes to H_2O^+) at its peak, but is concentrated more strongly near the nucleus and in the ion pile up region. This is because NH_4^+ is particularly sensitive to the increased ion transport further from the nucleus, and doesn't have time to be produced from ion-neutral chemistry when the bulk flow is too fast. NH_4^+ is also more strongly accelerated and reached higher velocities.

Figure 7 shows the total ion bulk velocity with arrows to show the direction of travel in each plane. Collisions are included for this simulation. Figures 7 [b], [d], and [f] show the same information as [a], [c] and [e], but focussed on the first 100 km from the nucleus. Panel [a] shows the bulk flow mainly diverted around the nucleus and tail-ward, with the radial motion only visible for 0–50 km from the nucleus. In the Y-Z plane (Figure 7f), where Rosetta was usually located, the radial flow extends over a larger region, up to 100 km.

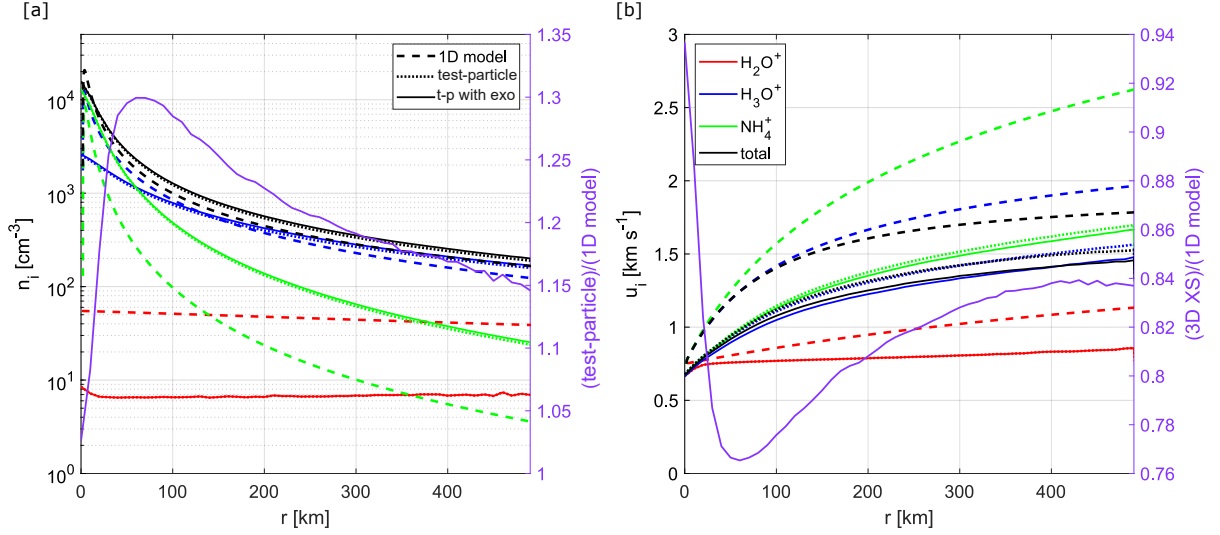


Figure 4. Comparison of 1D Ion Acceleration Model from Lewis et al. (2024) (dashed lines) with the 3D ion test-particle model with (solid lines) and without (dotted line) an exothermic energy release during protonation for [a] ion density and [b] ion bulk velocity. Profiles for H_2O^+ (red), H_3O^+ (blue) and NH_4^+ (green) are shown, alongside the total for all species (black). Right-hand axis shows the ratio between the two models for the total ion density (purple).

Figures 7 [c] and [e] show a strong component of the flow in the + Z direction, owing to the motional electric field.

4 COMPARISON WITH ROSETTA DATA

In this section, the modelled ion density is compared to the data from RPC-MIP and RPC-LAP. First, the full RPC-MIP/LAP combined dataset (Johansson et al. 2021) compared against the plasma density calculated by the field-free, chemistry-free model (Eq. 4) to verify where the model performs best over the Rosetta escort phase. This provides a reference case to compare with the ion test-particle model, to assess whether the plasma density can be constrained more accurately by the more complex model. In Section 4.2, the ion test-particle model is compared against the MIP/LAP dataset and the field-free, chemistry-free model.

4.1 MIP/LAP data vs field-free chemistry-free model

The MIP/LAP electron density data (Johansson et al. 2021) are first smoothed with a 1-minute rolling median to reduce noise and small-scale variations. Figure 8 shows the smoothed dataset sorted into 10 km bins of cometocentric distance and bins of width 0.1 of $\log_{10}(Qv^{\text{tot}})$. The median of each bin (Figure 8a) is shown, as well as the 25th percentile, as this value is less sensitive to electron density spikes, and may capture the baseline plasma density better. $Qv^{\text{tot}} [\text{s}^{-2}]$ is calculated from the local outgassing Q (from COPS and corrected for the neutral composition) and the total H_2O ionisation frequency (photoionisation and electron impact) from Stephenson et al. (2023).

Figure 8d then shows the field-free, chemistry-free model,

$$n_i(r) = \frac{Qv^{\text{tot}}}{4\pi u_n^2 r^2} (r - r_c), \quad (11)$$

which is equivalent to Eq. 4. The bulk neutral velocity u_n is known

to vary with heliocentric distance (Biver et al. 2019) as well as with cometocentric distance (Heritier et al. 2017b), but is assumed constant for Eq. 11. A value of $u_n = 700 \text{ km s}^{-1}$ is assumed, in line with the inputs to the ion test-particle model and hybrid simulation (Table 1). The colour scale in Figure 8d is capped at 500 cm^{-3} .

Figure 8c highlights the limitations of the parameter space we have for the Rosetta data. Despite its extensive escort phase, practical limitations mean that the coverage for low cometocentric distances at high outgassing is limited, and vice versa. However, it is possible to draw several conclusions from the data we do have. Figures 8e and 8f show the overestimation of the field-free chemistry-free model (Eq. 11) increases with ion production rate. At low outgassing, as predicted by Galand et al. (2016) and demonstrated in Galand et al. (2016) and Heritier et al. (2018), the field-free model performs well to explain the measured electron density (magenta). At high outgassing, where the conditions of the field-free chemistry-free model break, the observed electron density is up to 40 times higher than is calculated (colour scale in Figure 8e and 8f are capped at 10 for clarity). This has been previously reported in e.g. Vigren et al. (2019), but the full comparison over the whole escort phase is made here for the first time, using the full ionisation rates (photoionisation and electron-impact ionisation) as provided by Stephenson et al. (2023). Where the data are higher than the field-free chemistry-free model (shown in black in Figure 8e and f), this may be due to the changes in neutral composition at low outgassing. The CO_2 component of the coma was found to increase significantly over the southern hemisphere beyond 3.1 au (Gasc et al. 2017), which was shown in Galand et al. (2016) to increase the photoionisation rate by up to 50%.

The coverage of the parameter space in Figure 8 by previous studies is shown in Figure 9a, alongside the ion production rate Qv^{tot} used in this study (green line), and the instances of diamagnetic cavity crossings as detected by RPC-MAG (Goetz et al. 2016) (black crosses). Both the studies of Galand et al. (2016) (cyan triangles) and Heritier et al. (2018) (red squares) reported a good agreement between the field-free, chemistry-free model (Eq. 11) and the electron

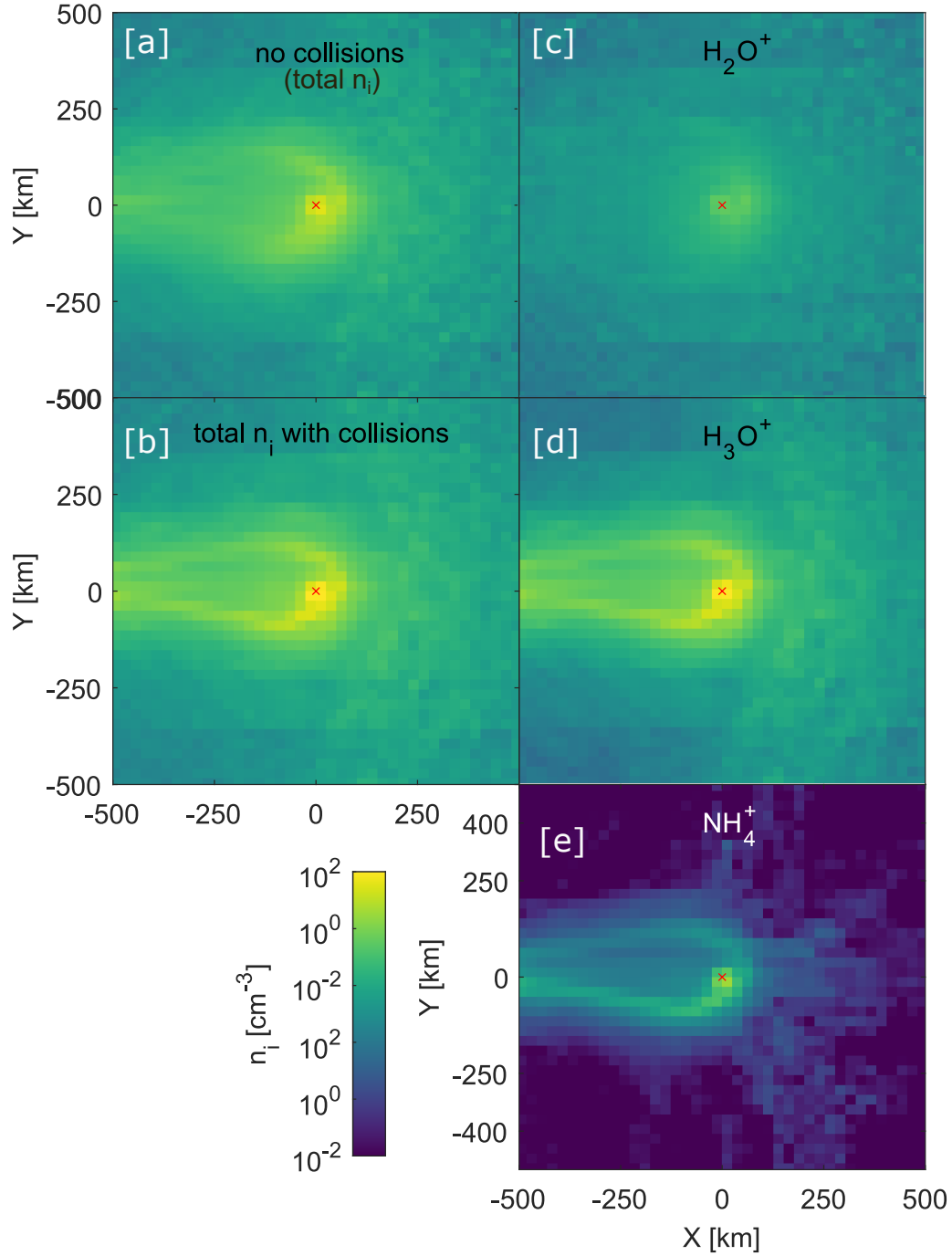


Figure 5. Ion density in the X-Y plane from the ion test-particle model, using the electric and magnetic fields from the AMITIS hybrid simulation (Table 1). [a] total ion density with no collisions, [b] total ion density with all collisions. For the collisional case, densities of [c] H_2O^+ , [d] H_3O^+ , and [e] NH_4^+ are given. The Sun is in the +X direction, and the comet nucleus is marked with a red cross.

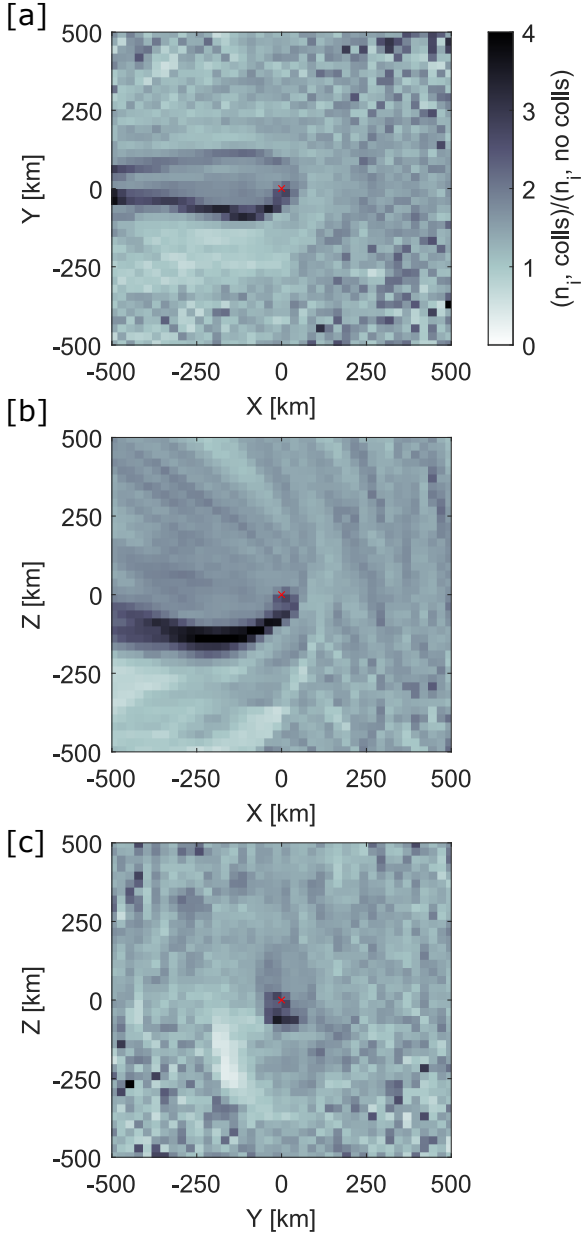


Figure 6. Ratio between the total ion densities calculated from the test-particle model with collisions included (as in Fig. 5b) and without (as in Fig. 5a). Red cross marks the location of the nucleus.

density data¹ in the low outgassing cases (for which the model was developed). The study of Vigren et al. (2019) (blue squares) applied Eq. 11 over a large time range post-perihelion, showing a transition from overestimation of the model near perihelion to good agreement at lower ion production rates. This result is well replicated in Figure 8, and generalised over the full dataset.

¹ Note that MIP and LAP were used separately in these studies as the combined MIP/LAP dataset (Johansson et al. 2021) was not yet available. This means that these studies include times when only one of the two datasets was available, which are not included in the combined dataset.

Figure 9b shows the location of the diamagnetic cavity boundary crossings as seen by RPC-MAG overlaid on Figure 8e. In general, the diamagnetic cavity has been observed for $Qv^{\text{tot}} > 1 \times 10^{20} \text{ s}^{-2}$, where Eq. 11 overestimates the plasma density. The larger the ion production rate, the further from the nucleus the cavity has been observed - however the data bias in the parameter space explored by Rosetta is probably artificially enhancing this trend.

The ion production rate $Qv^{\text{tot}} = 1.08 \times 10^{20} \text{ s}^{-2}$ used in the simulation in the hybrid simulation falls in an interesting region of the parameter space shown in Figure 9a. At cometocentric distances below 50 km, a generally good agreement with the field-free, chemistry-free model has been reported (Heritier et al. (2018) and in Figure 8). However, diamagnetic cavity crossings have also been observed at other times when Rosetta was closer to 100 km for the same Qv^{tot} . It is possible that this ion production rate reflects somewhat of a transition between the low outgassing regime, where the field-free chemistry-free model applies, and where the ambipolar electric field becomes important and leads to increased transport at the Rosetta distance.

4.2 MIP/LAP data vs test-particle model at 2.5-3 au

The plasma density from the ion test-particle model is now compared with the MIP/LAP combined dataset and the field-free chemistry-free model. The ion test-particle model and the AMITIS hybrid simulation only treat photoionisation, and do not include the electron-impact ionisation frequency. To account for this shortcoming of the models, both have artificially boosted the photoionisation frequency in accordance with the electron-impact ionisation frequency measured by RPC-IES (e.g., Stephenson et al. (2023)). The input parameters in Table 1 for the AMITIS model then represent the total ionisation frequency (v^{tot}) for the 2.5 – 3.0 au range. This total value is used in this Section for comparison with the Rosetta data. A more thorough implementation of electron-impact ionisation into the model is left for future work.

For comparison between the MIP/LAP data and the ion test-particle model run, simulated ions are used from the terminator (Y-Z) plane only. This is where Rosetta made the majority of its orbits around the comet, so is most applicable for data comparison. These simulated data are then averaged over 20 km radial bins and compared to the MIP/LAP data as presented in Figure 8, for $19.85 < \log_{10}(Qv^{\text{tot}}) < 20.15$. The result is shown in Figure 10. Even with the collisions implemented, the resulting ion densities are consistently lower than the plasma density measured by the spacecraft, by 5-10 times. The measured densities lie between the $u_i = u_n$ model (Eq. 11) and those calculated by the test-particle model, with good agreement between the data and the Eq. 11 particularly below 30 km. The reasons for the too low densities obtained by the test-particle model are discussed in Section 5, but it is clear that the cometary ions are transported too quickly in the hybrid model.

The ion bulk velocities for each of the species and the total from the test-particle model are shown in Figure 10b. It shows that the ions in the model are quickly accelerated to values significantly above the neutral speed, even in the first 20 km from the surface. The inclusion of collisions in the model decreases the bulk ion speed from 20 km s^{-1} to 11 km s^{-1} at 100 km. Despite the deceleration due to collisions, these speed values remain high, leading to underestimation of the plasma density compared with the observations. The reason for the high ion speeds is discussed in Section 5.3.2.

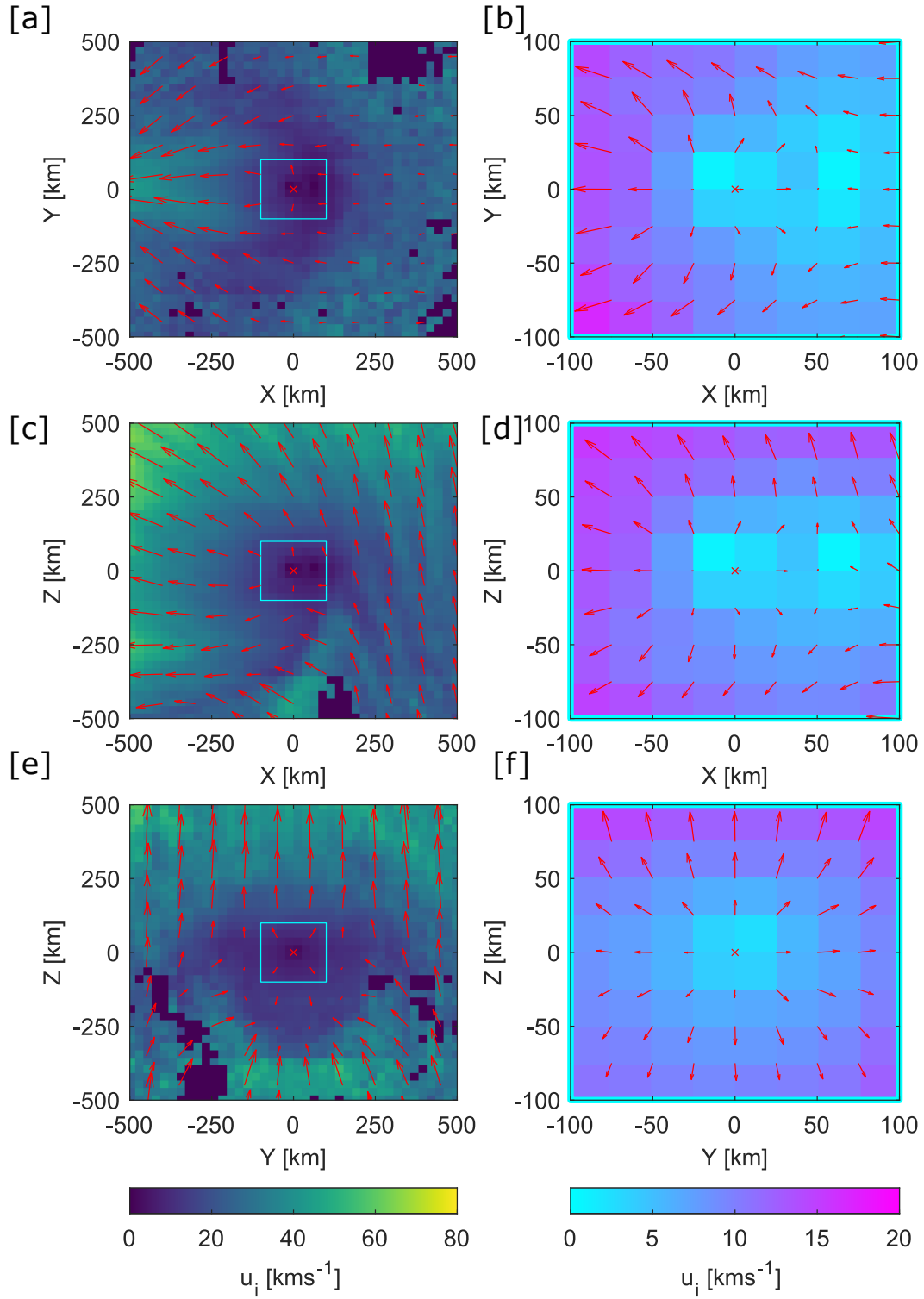


Figure 7. Ion bulk velocity magnitude (colour scale) and direction (red arrows) in the [a, b] X-Y plane, [c, d] X-Z plane, and [e, f] Y-Z plane, generated using the ion test-particle model with collisions included. Cyan box in left column corresponds to the 100×100 inset, shown in the right column. The comet nucleus is marked with a red cross.

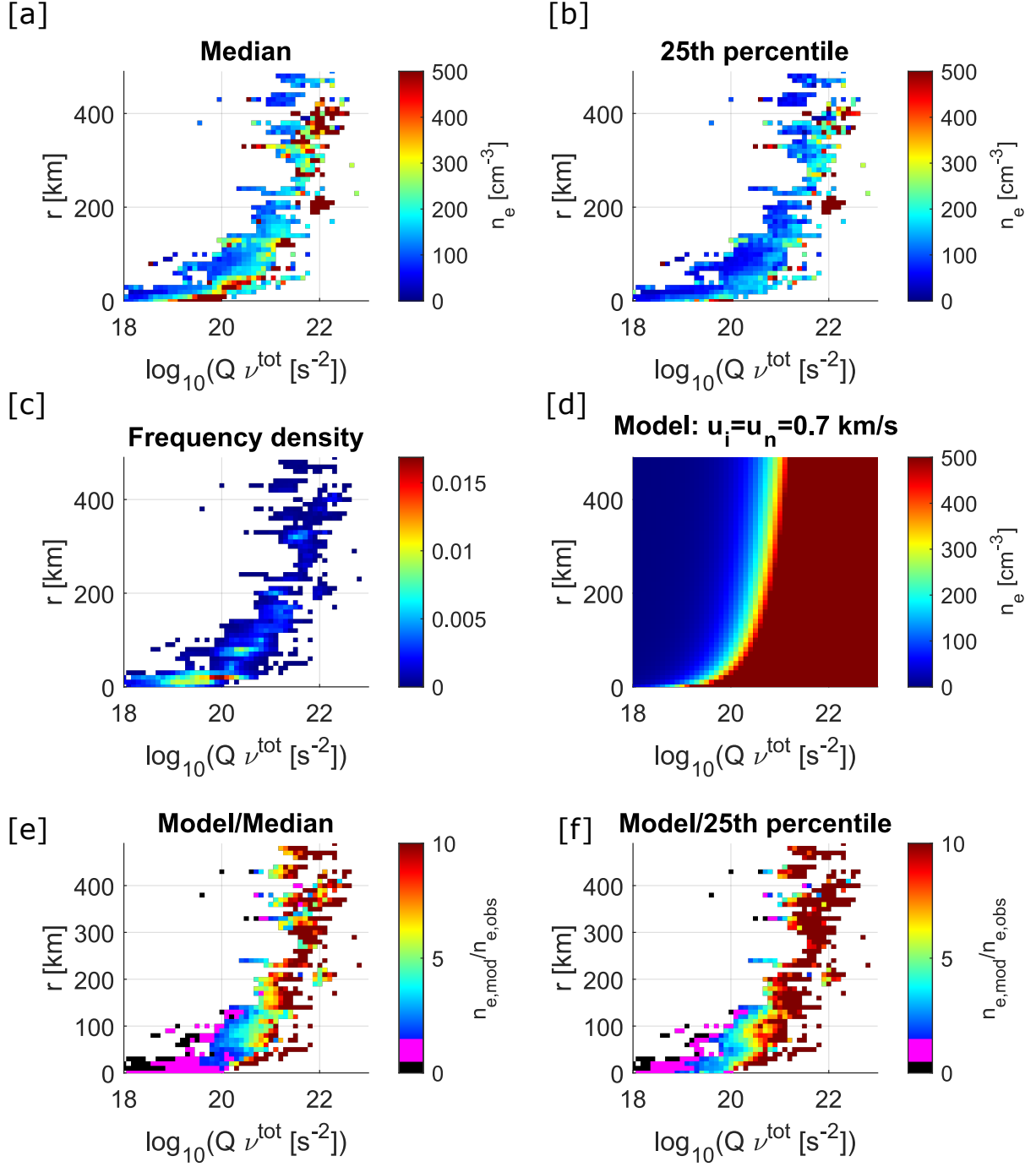


Figure 8. Heat maps showing the MIP/LAP combined dataset from the whole escort phase (covering August 2014– August 2016), binned by cometocentric distance r and $Q\nu^{\text{tot}}$. [a] Shows the median electron density in each bin, [b] shows the 25th percentile. [c] shows, for context, the frequency density of data in each bin. [d] Shows the density as calculated by the 1D field-free model (Eq. 11) and [e] and [f] the ratio between the field-free model and the MIP/LAP median and 25th percentiles respectively, with magenta indicating where the ratio is 0.5–1.5.

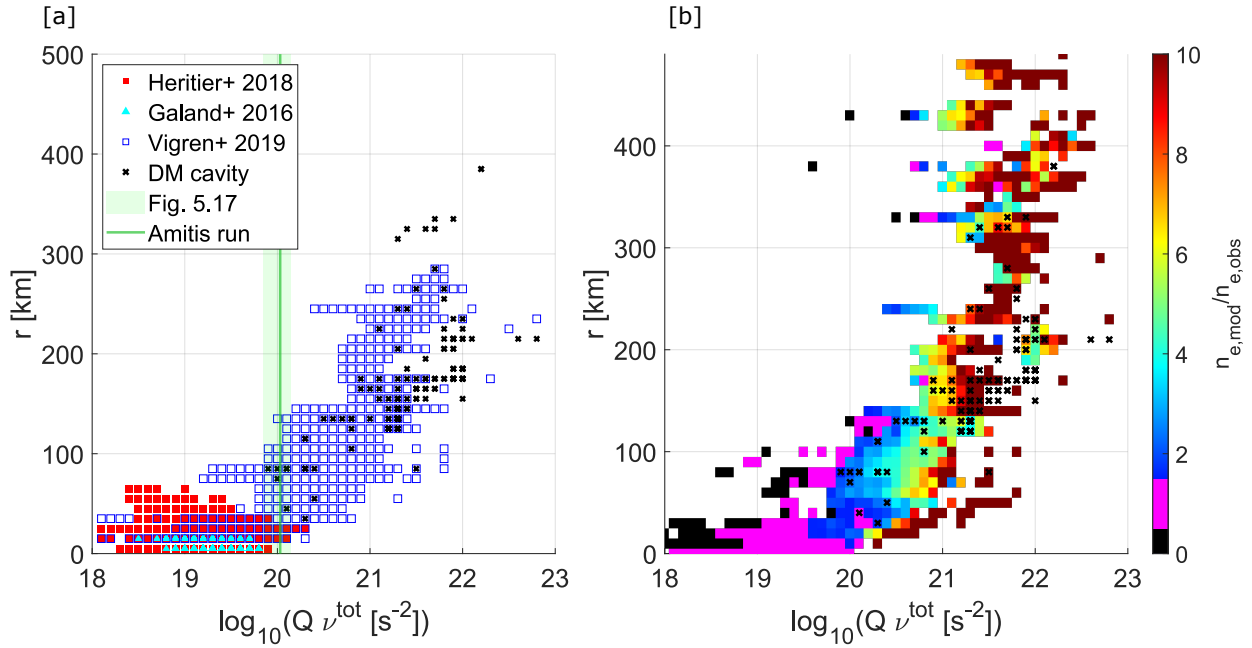


Figure 9. (a) Coverage of the parameter space in $Q \nu$ vs r (as in Figure 8), done by previous studies: Heritier et al. (2018) (red filled squares), Galand et al. (2016) (cyan triangles), and Vigren et al. (2019) (blue squares). The ion production rate $Q \nu$ from the hybrid simulation run is given by the green line, and the green shaded region is the data range used for MIP/LAP in Figure 8. The black crosses show diamagnetic cavity crossings as observed by RPC-MAG (Goetz et al. 2016) (b) Same as Figure 8e but with the diamagnetic cavity crossings marked with black crosses.

5 DISCUSSION

5.1 Impact of 1D fluid vs 3D kinetic collisions

In Section 2.3.1, the 3D test-particle model was applied to the radial electric field derived for the diamagnetic cavity crossings on 21st November 2015 in Lewis et al. (2024). It was shown that the energy-dependent 3D cross sections make the ion environment more collisional at this outgassing, driving more proton transfer and increasing the prevalence of NH_4^+ . However, the total $n_i u_i$ at a given cometocentric distance is preserved such that mean bulk ion velocity and electric field strengths required to reproduce the plasma density observed at Rosetta remain the same.

For the radial electric field case, the impact of the exothermic energy release during protonation was shown to be small but measurable, altering the total ion bulk speed by up to 8%. This is likely because the electric field and momentum transfer collisions quickly ‘fix’ the velocity back to being directed radially outwards from the nucleus. However, the exothermic energy release requires further study as it may have important implications for the ion dynamics at lower outgassing, when the electric field is weaker (Stephenson et al. 2024), though collisions are also less likely in this regime.

5.2 Application to intermediate outgassing

Applying the test-particle model to the electric and magnetic fields from the hybrid simulation AMITIS shows that the ion dynamics are different for individual ion species due to their different chemical pathways.

H_2O^+ is close to photochemical equilibrium, even at 2.5–3 au, so is present in low amounts and not concentrated in any particular location (see Figure 5c). Conversely, H_3O^+ and NH_4^+ are more strongly

affected by the electric fields, accumulating in greater numbers both near the nucleus and in the ion pile up region inside the magnetic pile up region (see Figure 5d-e). Collisions of all types are most effective in this ion pile up region, which extends into the comet tail. The chemistry is less complex in the +Z direction, that is, the direction of the motional electric field where transport is enhanced (see Figure 3).

It was previously assumed that the radial flow assumption was only valid in the diamagnetic cavity, when the only electric field term present was the ambipolar electric field. Figure 7 shows that within the first 100 km of the nucleus, radial motion dominates the flow in the Y-Z plane assessed by Rosetta (for conditions with no diamagnetic cavity). However, comparison with the MIP/LAP data suggests that the ions in the simulation may be accelerated too strongly, likely due to limitations of the hybrid model and the assumptions made about the electron temperature. This is discussed further in the next Section, 5.3.

Beyond 100 km, the flow is dominated upstream of the comet by the +Z component, accelerated by the motional electric field of the solar wind. On the anti-sunward side, the flow is tailward (-X), with the velocity direction in the -Z region corresponding to an electric field enhancement. This behaviour at large cometocentric distances is reported in detail by Moeslinger et al. (2024), so in this study, we focus mainly on the assessment of the cometary ion population at the spacecraft-comet distances covered by Rosetta at 2.5–3 au.

5.3 Comparison of the ion test-particle model and Rosetta data

In Section 4, the ion test-particle model was used to assess the impact of the electric and magnetic fields from the AMITIS hybrid simulation on the ion composition and density, and compared it to the equivalent plasma density observations from the combined MIP/LAP

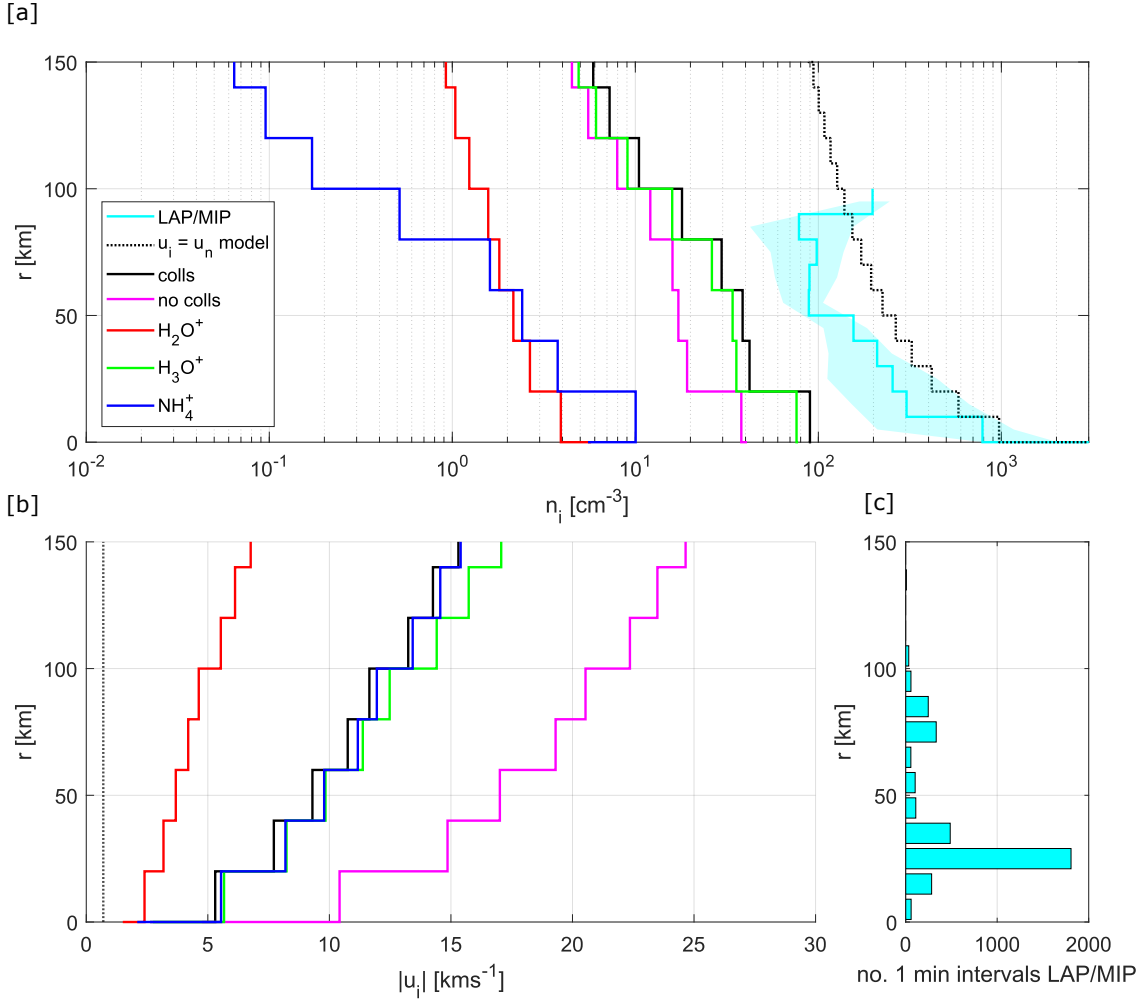


Figure 10. [a] Ion density averaged over 20 km cometocentric distance bins for the test-particle model in the terminator plane: Total with collisions (black), total without collisions (pink), H₂O⁺ (red), H₃O⁺ (green) and NH₄⁺ (blue). The field-free, chemistry-free modelled density using Eq. 11 is shown by the black dashed line. Cyan line shows the median in each radial bin from MIP/LAP for $19.85 < \log_{10}(Qv^{\text{tot}}) < 20.15$. Shaded region shows the 25th-75th percentile range of the data in each bin. [b] same as [a] but for the ion bulk velocity from the test-particle model only. [c] Number of 1-minute intervals in each 10 km bin for the MIP/LAP dataset.

dataset. The input conditions (Table 1) used were representative of those witnessed by Rosetta at 2.5 – 3 au post-perihelion.

The key finding of this comparison is that the plasma density data at this outgassing ($\sim 1.5 \times 10^{26} \text{ s}^{-1}$) are underestimated by the test-particle model, even with collisions slowing the acceleration by the electric fields. In fact, the bulk of the data lie somewhere between the profile calculated by the 3D model and the one calculated by the field-free, chemistry-free model (which assumes $u_i = u_i = 0.7 \text{ km s}^{-1}$, Eq. 11, see Figure 10). To understand the underestimation of the plasma density by the model, we need to reflect on the assumptions made in both the test-particle model and the hybrid electric and magnetic fields that drive it.

5.3.1 Electron-impact ionisation

In the hybrid simulations, photoionisation and charge exchange with the solar wind are considered. Electron-impact ionisation is not modelled, only treated by boosting the photoionisation, because its proper assessment requires the kinetic treatment of electrons.

In an optically thin coma the photoionisation frequency is broadly constant with radial distance but this may not be the case for the electron impact. Stephenson et al. (2023) modelled the solar wind and cometary electrons using the collisional test-particle model. They showed that the electron-impact ionisation frequency, primarily due to accelerated solar wind electrons and their secondaries, was enhanced at an outgassing of 10^{26} s^{-1} in the first 100 km from the nucleus. This suggests that simple ‘boosting’ of the photoionisation frequency to account for electron impact (informed by the data from

(Stephenson et al. (2023)) is unlikely to capture the full radial profile of the ion production rate properly.

However, multi-instrument analysis of far-ultraviolet emission using in-situ electron impact frequencies for dissociative excitation (assumed to be independent of cometocentric distance) has shown to produce simulated brightnesses consistent with observations (Stephenson et al. (2021), Galand et al. (2020)). This suggests that a spatially-uniform electron-impact ionisation frequency, for uniform neutral outgassing, as assumed here, is likely to be a reasonable assumption.

5.3.2 Electron temperature

The collisionality of electrons observed near the nucleus raises further questions about the validity of the hybrid simulation and its fluid treatment of the electrons. The electrons are assumed to be adiabatic, such that

$$p_e = n_e k_B T_e = \alpha n_e^\gamma \quad (12)$$

and

$$T_e = T_{e,SW} \left(\frac{n_e}{n_{e,sw}} \right)^{\gamma-1} \quad (13)$$

where p_e is the total thermal pressure of the electrons, and $\alpha = k_B n_{e,sw}^{1-\gamma} T_{e,sw}$ where $n_{e,sw}$ and $T_{e,sw}$ are the number density and temperature of the electrons in the solar wind, respectively (fixed in the inputs of the simulations). γ is the adiabatic index, assumed 5/3 (three degrees of freedom for monatomic gas). In the solar wind, or at low enough neutral density (i.e. sufficiently far from the nucleus), this treatment of the electrons as one population with a Maxwellian distribution may be reasonable, but is clearly an oversimplification in the inner coma. In this region, the cometary electrons have distinct populations according to the collisions and field acceleration they undergo, and, beside a warm e^- population ($\sim 5-10$ eV), a significant population of cold electrons was observed throughout the Rosetta escort (Gilet et al. 2020).

Stephenson et al. (2023) showed using their 3D electron test-particle model, that the electron-neutral collisions produce cold electrons and a ‘flattened’ potential well in the collisional region surrounding the nucleus. Neglect of this collisional cooling is a serious limitation of the hybrid simulations that are based on the adiabatic temperature assumption. Such an assumption leads to a very high \vec{E}_{amb} , hence high ion speeds and low ion densities. For the model runs in Section 4, a lower ambipolar electric field strength near the surface would result in less acceleration of the cometary ions. That is, slower bulk velocity and higher densities - perhaps closer to the measured plasma densities from MIP/LAP. A similar observation was made in Koenders et al. (2015), who solved the electron pressure equation in place of the adiabatic assumption, noting by comparison to Koenders et al. (2013) (who used an adiabatic pressure) that the latter caused an additional force on the ions in the inner coma.

The collisionality of the electrons may therefore be key to understand why the radial $u_i = u_n$ model works so well at low outgassing. However, the impact of the electron-neutral collisions at higher outgassing cannot be determined without a fully kinetic and collisional 3D model of electrons and self-consistent fields.

6 CONCLUSIONS

In Section 2.3.1, we showed that for a radial electric field (and no magnetic field, as inside the diamagnetic cavity) the 3D collisional

cross sections lead to up to 20% more collisions than the 1D kinetic rates used in Lewis et al. (2024). However the same bulk velocity, hence the same ambipolar field, is required to explain the electron density measured by Rosetta.

By assessing the effect of its inclusion in the ion test-particle model, it was demonstrated that the exothermic energy released in protonation reactions only plays a minor role in the ion dynamics near perihelion. It is possible, however, that this energy release may have more consequences when the electric fields applied are weaker.

In Section 3, the ion test-particle model was applied to input conditions representative of comet 67P at 2.5-3 au, and driven by hybrid electric and magnetic fields produced by the Amitis simulation (see Section 2.2). For this lower outgassing ($Q = 5.4 \times 10^{26} \text{ s}^{-1}$), when no diamagnetic cavity has formed, cometary ions still move predominantly radially, up to 100 km above the surface. H_2O^+ is close to photochemical equilibrium, while H_3O^+ and NH_4^+ are strongly affected by the strong ambipolar electric and magnetic fields generated by the hybrid simulation.

Finally, in Section 4 we compare the total plasma density from the ion test-particle model with the in situ data from Rosetta. Even with collisions, the total plasma density derived by the test-particle model is low compared to the MIP/LAP data at the same outgassing. This seems to result from the assumption of adiabatic electrons driving strong ambipolar electric fields in the hybrid simulations, and therefore overestimating the loss of ions through transport. This highlights that kinetic, collisional modelling of the cometary electrons are necessary to understand the ion dynamics and chemistry fully.

ACKNOWLEDGEMENTS

We would like to acknowledge the invaluable work of the RPC team, the whole ESA Rosetta team, and the ESA Planetary Science Archive team. Work at Imperial College London was supported by the Science and Technology Facilities Council (STFC) of the UK under studentship ST/W507519/1 and grant ST/W001071/1, and by the UK Space Agency (UKSA) under grant ST/X002349/1.

DATA AVAILABILITY

The data used in this article are available on the Planetary Science Archive at <https://psa.esa.int>. The AMITIS simulation results used in this work are available at Moeslinger & Gunell (2024).

REFERENCES

- Altwegg K., et al., 1993, *Astronomy and Astrophysics*, 279, 260
- Balsiger H., et al., 2007, *Space Science Reviews*, 128, 745
- Bergman S., et al., 2021a, *Monthly Notices of the Royal Astronomical Society*, 503, 2733
- Bergman S., Stenberg Wieser G., Wieser M., Nilsson H., Vigren E., Beth A., Masunaga K., Eriksson A., 2021b, *Monthly Notices of the Royal Astronomical Society*, 507, 4900
- Beth A., Galand M., 2017, *Monthly Notices of the Royal Astronomical Society*, 469, S824
- Beth A., et al., 2016, *Monthly Notices of the Royal Astronomical Society*, 462, S562
- Beth A., Galand M., Heritier K. L., 2019, *Astronomy and Astrophysics*, 630
- Biver N., et al., 2019, *Astronomy and Astrophysics*, 630
- Carr C., et al., 2007, *Space Science Reviews*, 128, 629
- Deca J., Divin A., Henri P., Eriksson A., Markidis S., Olshevsky V., HorÁnyi M., 2017, *Physical Review Letters*, 118

Deca J., Henri P., Divin A., Eriksson A., Galand M., Beth A., Ostaszewski K., Horányi M., 2019, *Physical Review Letters*, 123, 055101

Eriksson A. I., et al., 2007, *Space Science Reviews*, 128, 729

Fahr H., Mueller K. G., 1967, *Zeitschrift für Physik*, 200, 343

Fatemi S., Poppe A. R., Delory G. T., Farrell W. M., 2017, *Journal of Physics: Conference Series*, 837, 012017

Fleshman B. L., Delamere P. A., Bagenal F., Cassidy T., 2012, *J. Geophys. Res.*, 117

Galand M., et al., 2016, *Monthly Notices of the Royal Astronomical Society*, 462, S331

Galand M., et al., 2020, *Nature Astronomy*, 4, 1084

Gasc S., et al., 2017, *Monthly Notices of the Royal Astronomical Society*, 469, S108

Gilet N., et al., 2020, *Astronomy and Astrophysics*, 640

Glassmeier K.-H., Boehnhardt H., Koschny D., Kührt E., Richter I., 2007a, *Space Science Reviews*, 128, 1

Glassmeier K. H., et al., 2007b, *Space Science Reviews*, 128, 649

Goetz C., et al., 2016, *Monthly Notices of the Royal Astronomical Society*, 462, S459

Gunell H., Lindkvist J., Goetz C., Nilsson H., Hamrin M., 2019, *Astronomy and Astrophysics*, 631

Hansen K. C., et al., 2016, *Monthly Notices of the Royal Astronomical Society*, 462, S491

Haser L., 1957, *Bulletin de la Classe des Sciences de l'Académie Royale de Belgique*, 43, 740

Heritier K. L., et al., 2017a, *Monthly Notices of the Royal Astronomical Society*, 469, S118

Heritier K. L., et al., 2017b, *Monthly Notices of the Royal Astronomical Society*, 469, S427

Heritier K. L., et al., 2018, *Astronomy and Astrophysics*, 618

Hunter E. P. L., Lias S. G., 1998, *Journal of Physical and Chemical Reference Data*, 27, 413

Johansson F. L., et al., 2021, *Astronomy & Astrophysics*, 653, A128

Koenders C., Glassmeier K. H., Richter I., Motschmann U., Rubin M., 2013, *Planetary and Space Science*, 87, 85

Koenders C., Glassmeier K. H., Richter I., Ranocha H., Motschmann U., 2015, *Planetary and Space Science*, 105, 101

Lewis Z. M., et al., 2023, *Monthly Notices of the Royal Astronomical Society*, 523, 6208

Lewis Z. M., Beth A., Galand M., Henri P., Rubin M., Stephenson P., 2024, *Monthly Notices of the Royal Astronomical Society*, 530, 66

Marshall D. W., et al., 2017, *Astronomy & Astrophysics*, 603, A87

Moeslinger A., Gunell H., 2024, *Particle Tracing Code*, doi:10.5281/ZENODO.10973547, <https://zenodo.org/doi/10.5281/zenodo.10973547>

Moeslinger A., Gunell H., Nilsson H., Fatemi S., Stenberg Wieser G., 2024, *Journal of Geophysical Research: Space Physics*, 129, e2024JA032757

Murad E., Bochsler P., 1987, *Nature*, 326, 366

Odelstad E., Stenberg-Wieser G., Wieser M., Eriksson A. I., Nilsson H., Johansson F. L., 2017, *Monthly Notices of the Royal Astronomical Society*, 469, S568

Odelstad E., et al., 2018, *Journal of Geophysical Research: Space Physics*, 123, 5870

Stephenson P., et al., 2021, *Astronomy and Astrophysics*, 647

Stephenson P., Galand M., Deca J., Henri P., Carnielli G., 2022, *MNRAS*, 511, 4090

Stephenson P., et al., 2023, *Monthly Notices of the Royal Astronomical Society*, 525, 5041

Stephenson P., Galand M., Deca J., Henri P., 2024, *Monthly Notices of the Royal Astronomical Society*, 529, 2854

Trotignon J. G., et al., 2007, *Space Science Reviews*, 128, 713

Vigren E., Eriksson A. I., 2017, *The Astronomical Journal*, 153, 150

Vigren E., Galand M., 2013, *Astrophysical Journal*, 772

Vigren E., et al., 2017, *MNRAS*, 469, 142

Vigren E., et al., 2019, *The Astrophysical Journal*, 881, 6

Williamson H. N., Johansson A., Canu-Blot R., Stenberg-Wieser G., Nilsson H., Johansson F. L., Moeslinger A., 2024, *Monthly Notices of the Royal Astronomical Society*, 533, 1442

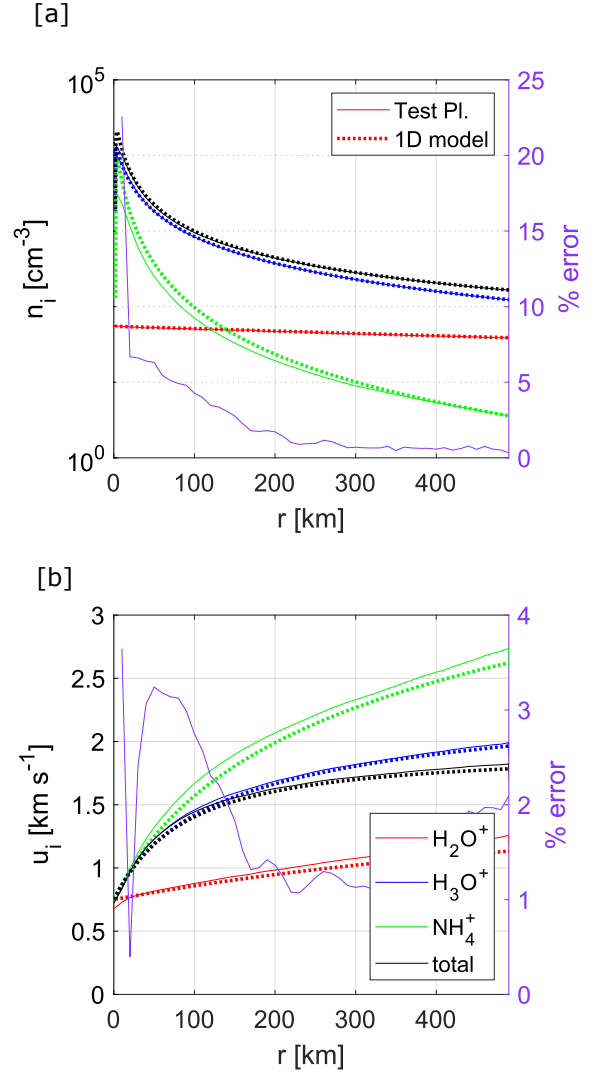


Figure A1. [a] H₂O⁺ (red), H₃O⁺ (blue), NH₄⁺ (green) and total (black) density profiles from the 1D Ion Acceleration Model described in Lewis et al. (2024) (dotted lines) compared with those from the test-particle model (solid lines). [b] same as [a] but for the bulk ion velocity. Input parameters are given in Table 2

APPENDIX A: VALIDATION OF THE TEST-PARTICLE MODEL

A1 Radial electric fields with collisions

Here the collisional aspect of the ion test-particle model is validated, without the hybrid electric and magnetic field input. Figure A1 shows the comparison of the ion test-particle model (Section 2) with the 1D ion acceleration model presented in Lewis et al. (2024). Models are both run using the same electric field profile (radial and proportional to $1/r$) and using the input parameters given in Table 2.

A2 Collisionless case

In Figure A2, The test-particle model is now validated in the collisionless case against the output cometary ion density from AMITIS (Moeslinger et al. 2024). The input parameters are given in Table 1.

APPENDIX B: ION-NEUTRAL COLLISION CROSS SECTIONS

This paper has been typeset from a \LaTeX file prepared by the author.

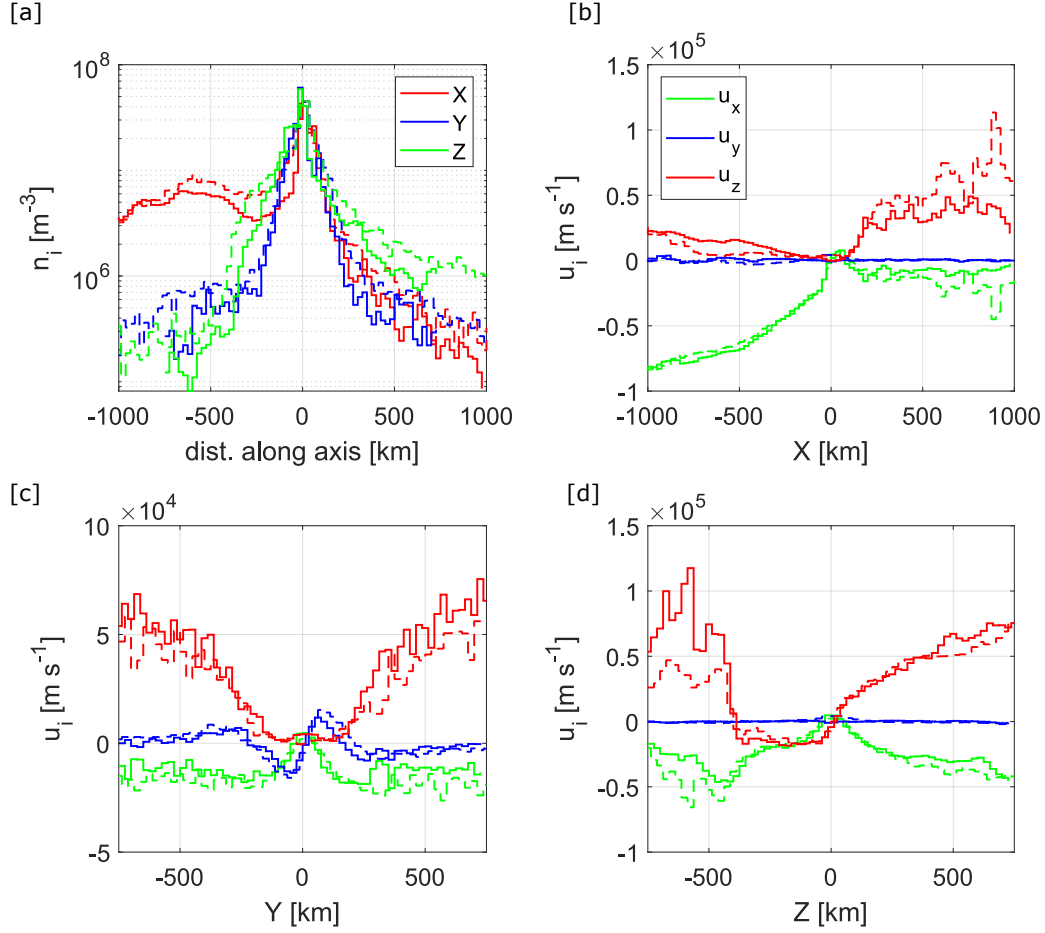


Figure A2. Comparison of the test-particle model described in Section 2.1 with collisions removed (solid lines), and the AMITIS collisionless hybrid simulation (dashed lines). [a] Total ion density along the X, Y and Z axis. [b-d], X (green), Y (blue) and Z (red) components of the bulk ion velocity along each axis. The sun is in the +X direction, with the interplanetary magnetic field in the +Y direction.

Reaction type	Equation	Cross section [10^{-16} cm^2]	Range [eV]	Reference
Proton transfer	$\text{H}_2\text{O}^+ + \text{H}_2\text{O} \rightarrow \text{H}_3\text{O}^+ + \text{OH}$	$\sigma(E_{\text{rel}}) = 38E_{\text{rel}}^{-0.88} - 0.39 \exp\left[-0.5\left(\frac{E_{\text{rel}}-57}{12}\right)^2\right]$	0.1 - 100	Fleshman et al. (2012)
Proton transfer	$\text{H}_2\text{O}^+ + \text{NH}_3 \rightarrow \text{NH}_4^+ + \text{OH}$	$\sigma(E_{\text{rel}}) = 38E_{\text{rel}}^{-0.88} - 0.39 \exp\left[-0.5\left(\frac{E_{\text{rel}}-57}{12}\right)^2\right]$	0.1 - 100	Fleshman et al. (2012)
Proton transfer	$\text{H}_3\text{O}^+ + \text{NH}_3 \rightarrow \text{NH}_4^+ + \text{H}_2\text{O}$	$\sigma(E_{\text{rel}}) = 38E_{\text{rel}}^{-0.88} - 0.39 \exp\left[-0.5\left(\frac{E_{\text{rel}}-57}{12}\right)^2\right]$	0.1 - 100	Fleshman et al. (2012)
Momentum transfer	$\text{H}_2\text{O}^+ + \text{H}_2\text{O} \rightarrow \text{H}_2\text{O}^+ + \text{H}_2\text{O}$	$\sigma(E_{\text{rel}}) = 24E_{\text{rel}}^{-0.5}$	Not given	Vigren & Eriksson (2017)
Momentum transfer	$\text{H}_3\text{O}^+ + \text{H}_2\text{O} \rightarrow \text{H}_3\text{O}^+ + \text{H}_2\text{O}$	$\sigma(E_{\text{rel}}) = 24E_{\text{rel}}^{-0.5}$	Not given	Vigren & Eriksson (2017)
Momentum transfer	$\text{NH}_4^+ + \text{H}_2\text{O} \rightarrow \text{NH}_4^+ + \text{H}_2\text{O}$	$\sigma(E_{\text{rel}}) = 24E_{\text{rel}}^{-0.5}$	Not given	Vigren & Eriksson (2017)
Electron transfer	$\text{H}_2\text{O}^+ + \text{H}_2\text{O} \rightarrow \text{H}_2\text{O}^+ + \text{H}_2\text{O}$	$\sigma(E_{\text{rel}}) = 38E_{\text{rel}}^{-0.5}$	0.1 - 100	Fleshman et al. (2012)

Table B1. Ion-neutral collision cross sections used in the test-particle model